Classical density functional theory for interfacial properties of hydrogen, helium, deuterium, neon and their mixtures

Morten Hammer,[1,2,3] Gernot Bauer,[3] Rolf Stierle,[3] Joachim Gross,[3] and Øivind Wilhelmsen[1,2,3,a]

[1)]*Porelab, Department of Chemistry, Norwegian University of Science and Technology, NO-7491 Trondheim, Norway*

[2)]*Department of Gas Technology, SINTEF Energy Research, NO-7465 Trondheim, Norway*

[3)]*Institute of Thermodynamics and Thermal Process Engineering, University of Stuttgart, Pfaffenwaldring 9, D-70569 Stuttgart, Germany*

(Dated: 20 February 2023)

We present a classical density functional theory (DFT) for fluid mixtures that is based on a third-order thermodynamic perturbation theory of Feynman-Hibbs corrected Mie potentials. The DFT is developed to study the interfacial properties of hydrogen, helium, neon, deuterium and their mixtures, i.e., fluids that are strongly influenced by quantum effects at low temperatures. White Bear fundamental measure theory is used for the hard-sphere contribution of the Helmholtz energy functional, and a weighted density approximation is used for the dispersion contribution. For mixtures, a contribution is included to account for non-additivity in the Lorentz-Berthelot combination rule. Predictions of the radial distribution function from DFT are in excellent agreement with results from molecular simulations, both for pure components and mixtures. Above the normal boiling point and 5% below the critical temperature, the DFT yields surface tensions of neon, hydrogen, and deuterium with average deviations from experiments of 7.5%, 4.4%, and 1.8% respectively. The surface tensions of hydrogen/deuterium, para-hydrogen/helium, deuterium/helium, and hydrogen/neon mixtures are reproduced with a mean absolute error of 5.4%, 8.1%, 1.3%, and 7.5%, respectively. The surface tensions are predicted with excellent accuracy at temperatures above $20\,\mathrm{K}$. The poor accuracy below $20\,\mathrm{K}$ is due to the inability of Feynman–Hibbs corrected Mie potentials to represent the real fluid behavior at these conditions, motivating the development of new intermolecular potentials. This DFT can be leveraged in the future to study confined fluids and assess the performance of porous materials for hydrogen storage and transport.

I. INTRODUCTION

Vapor-liquid equilibria of fluids such as neon, helium, hydrogen and deuterium occur at temperatures below $60\,\mathrm{K}$, where other compounds form solids. At these temperatures, quantum effects make significant contributions to the surface tension,[1,2] as well as other interfacial properties.[3]

It has become increasingly relevant to understand how quantum effects influence interfacial properties. Liquefaction at approximately $20\,\mathrm{K}$ is a promising concept for large-scale distribution of hydrogen over longer distances.[4] Mixed refrigerants of hydrogen, helium, and neon can potentially be used to increase the efficiency of the energy-intensive hydrogen liquefaction process. The surface tension is a key parameter to estimate condensation (and evaporation) rates of refrigerants, which are needed to design heat exchangers.[5–7]

Other applications also require a model capturing quantum effects for the description of interfacial phenomena, such as hydrogen isotope separation technologies for deuterium production,[8] the exotic behavior of helium droplets,[9] and the storage of hydrogen in metal-organic frameworks and zeolites.[10]

The importance of quantum effects relative to the classical behavior of fluids can be estimated by comparing the de Broglie wavelength, $\Lambda = h/\sqrt{2\pi m k_{\mathrm{B}} T}$, to the typical length scale across which molecules interact, where h and k_{B} are Planck's and Boltzmann's constants, m is the molecular mass, and T is the temperature. The de Broglie wavelength increases with decreasing temperature and molecular mass, which explains why hydrogen and helium have particularly strong quantum effects. Quantum effects are also important at high densities.[11] Although solutions of the Schrödinger equation can be used to calculate the properties of such fluids, this is currently computationally unfeasible for systems consisting of a sufficiently large number of molecules to study vapor-liquid interfaces. Hence, there is a need for approximate methods. A formally exact method to model the full quantum behavior of an interaction potential is the path integral Monte Carlo approach.[12–14] Wang and Johnson[15] used this method to calculate the phase equilibrium of hydrogen and neon, which was in good agreement with experimental data. In practice however, a simpler *semi-classical* approach based on pair potentials is often preferred.[16]

Wigner–Kirkwood theory[17,18] was the first to describe semi-classical, temperature-dependent quantum corrections to classical interaction potentials. Feynman and Hibbs later used another route to re-derive such quantum corrections,[19] which to first order are equivalent with the Wigner–Kirkwood theory. They have later been

[a)]Electronic mail: oivind.wilhelmsen@ntnu.no

referred to as *Feynman–Hibbs corrections*.[19] The underlying idea is that classical statistical mechanics could be used to study fluids influenced by quantum effects by using *quantum-corrected*, temperature-dependent pair potentials.[19] This is particularly useful in molecular simulations, where fluids can be studied at low temperatures using these semi-classical potentials. This simulation approach has been used to study phenomena such as the adsorption of hydrogen in porous materials,[10,20] quantum clusters,[21,22] helium at low temperatures,[23] and quantum fluids under confinement.[24]

In recent work,[25–27] we have shown that Feynman–Hibbs corrected Mie potentials with appropriately regressed parameters are capable of representing the thermodynamic properties of hydrogen, helium, deuterium, neon, and their mixtures at temperatures above 20 K. A third-order perturbation theory was developed called statistical associating fluid theory of quantum corrected Mie potentials (SAFT-VRQ Mie).[25,26] It was shown to be in excellent agreement with results from both molecular simulations and experiments. We will use the SAFT-VRQ Mie equation of state (EoS) as basis to develop a classical density functional theory (DFT) for Feynman–Hibbs corrected Mie potentials.

In previous works, DFT and molecular simulations have been used with great success to estimate a range of important interfacial properties of classical fluids, such as the surface tension[28] and its curvature dependence,[29,30] interfacial resistivities,[31–33] and adsorption isotherms.[34] The goal of the present work is to investigate whether Feynman–Hibbs corrected Mie potentials can provide a pathway to achieve the same for fluids that are strongly influenced by quantum effects.

Our development of a DFT for fluids influenced by quantum effects follows along the same lines as previous work on DFT for classical fluids,[35] which has been shown to accurately represent the surface tension[36,37] and adsorption isotherms of confined systems.[34] We find it necessary to extend the Helmholtz energy functional with an additional contribution that accounts for non-additivity in the Lorentz-Berthelot combination rule to capture the behavior of helium-hydrogen and helium-deuterium mixtures.[38,39]

We demonstrate that the presented DFT provides accurate *predictions* of the surface tensions of both pure fluids and mixtures that exhibit strong quantum effects at temperatures above 20 K. By comparing with results from molecular simulations, we also show that the DFT is able to represent the radial distribution function of both single-component fluids and mixtures described by Feynman–Hibbs corrected Mie potentials. The DFT extends the simulation-theory-experiment nexus provided by the SAFT-VRQ Mie EoS to inhomogeneous systems.

The paper is structured as follows. In Sec. II we introduce a DFT that is based on the the SAFT-VRQ Mie EoS. Details on numerical solution of the DFT and molecular simulations are provided in Sec. III. In Sec. IV we compare predictions from the DFT to experimental surface tensions of pure components and mixtures, as well as the radial distribution function of Mie Fluids from molecular simulations. Concluding remarks are provided in Sec. V.
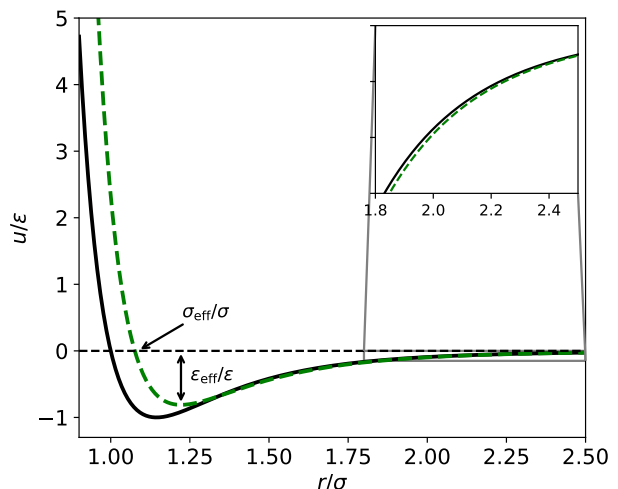

FIG. 1: Comparison of the classical Mie interaction potential (black, solid line) and the Feynman–Hibbs corrected Mie-potential (green, dashed) of hydrogen, at reduced temperature $T^* = 1$. The Feynman–Hibbs correction increases the effective diameter σ_{eff}, and decreases the well depth ϵ_{eff}, compared to the classical Mie parameters σ and ϵ.

II. THEORY

This section presents a DFT for Feynman–Hibbs corrected Mie potentials. We restrict the discussion to first-order Feynman–Hibbs corrected Mie potentials, since they have been shown to give the best overall performance.[25,26] The expression for the interaction potential between interaction sites of type i and j is

$$\frac{u_{ij}(r_{ij})}{\mathcal{C}(\lambda_{r,ij}, \lambda_{a,ij})\epsilon_{ij}} = \frac{\sigma_{ij}^{\lambda_{r,ij}}}{r_{ij}^{\lambda_{r,ij}}} - \frac{\sigma_{ij}^{\lambda_{a,ij}}}{r_{ij}^{\lambda_{a,ij}}}$$
$$+ \frac{\beta\hbar^2}{24m_{ij}}\left(Q_1(\lambda_{r,ij})\frac{\sigma_{ij}^{\lambda_{r,ij}}}{r_{ij}^{\lambda_{r,ij}+2}} - Q_1(\lambda_{a,ij})\frac{\sigma_{ij}^{\lambda_{a,ij}}}{r_{ij}^{\lambda_{a,ij}+2}}\right), \quad (1)$$

where the potential well-depth is ϵ_{ij}, the characteristic length scale corresponding to the distance at which the inter-molecular *Mie potential* is zero is σ_{ij}, and the attractive and repulsive exponents are $\lambda_{a,ij}$ and $\lambda_{r,ij}$, respectively. $\hbar = \frac{h}{2\pi}$ is the reduced Planck's constant. The factors $\mathcal{C}$ and Q_1 are

$$\mathcal{C}(\lambda_r, \lambda_a) = \left(\frac{\lambda_r}{\lambda_r - \lambda_a}\right)\left(\frac{\lambda_r}{\lambda_a}\right)^{\frac{\lambda_a}{\lambda_r - \lambda_a}}, \quad (2)$$

and

$$Q_1(\lambda) = \lambda(\lambda - 1).\qquad(3)$$

The Feynman–Hibbs correction is given as the second line of Eq. (1). It introduces a temperature- and mass-dependent prefactor, where the expression in the parentheses is the second derivative of the Mie potential with respect to the inter-molecular distance, r_{ij}.[19,25]

As the temperature decreases, the first-order correction 1) increases the effective size-parameter $\sigma_{ij,\mathrm{eff}}$ and 2) decreases the effective potential well-depth $\epsilon_{ij,\mathrm{eff}}$. These effects are illustrated in Fig. 1. At high temperatures, the first-order contribution becomes negligible and the classical Mie potential is restored.

The following relationships are used as combination rules for the molecular potential parameters[40]

$$\sigma_{ij} = \frac{1}{2}\left(\sigma_{ii} + \sigma_{jj}\right)\left(1 - l_{ij}\right),\qquad(4a)$$

$$\epsilon_{ij} = (1 - k_{ij})\frac{\sqrt{\sigma_{ii}^3\sigma_{jj}^3}}{\sigma_{ij}^3}\sqrt{\epsilon_{ii}\epsilon_{jj}},\qquad(4b)$$

$$\lambda_{ij} - 3 = \sqrt{\left(\lambda_{ii} - 3\right)\left(\lambda_{jj} - 3\right)},\qquad(4c)$$

$$\frac{1}{m_{ij}} = \frac{1}{m_i} + \frac{1}{m_j},\qquad(4d)$$

where l_{ij} and k_{ij} are binary correction parameters for the diameter-parameter and well-depth parameter, respectively. These parameters have been regressed in previous work by using experimental data of binary phase equilibria.[26]

In two previous works,[25,26] we presented the SAFT-VRQ Mie EoS, which represents the thermodynamic properties of fluids interacting via Feynman–Hibbs corrected Mie potentials. For mixtures, the specific reduced Helmholtz energy is:

$$a^{\mathrm{res}} = a - a^{\mathrm{ig}} = a^{\mathrm{hs}} + a^{\mathrm{nad}} + a^{\mathrm{disp}},\qquad(5)$$

where $A = aNk_{\mathrm{B}}T$ is the total Helmholtz energy, and superscripts ig, res, hs, nad and disp refer to the ideal-gas, residual, hard-sphere, non-additive, and dispersion contributions, respectively. The SAFT-VRQ Mie EoS is valid for bulk-phases. We shall next elaborate how the thermodynamic description can be extended to heterogeneous systems with DFT.

A. DFT with the SAFT-VRQ Mie Equation of State

The starting point of DFT is the grand canonical functional,

$$\Omega\left[\{\rho_i(\mathbf{r})\}\right] = F\left[\{\rho_i(\mathbf{r})\}\right] + \sum_i^{N_c}\int \mathrm{d}\mathbf{r}\,\rho_i(\mathbf{r})\left(V_i^{\mathrm{ext}}(\mathbf{r}) - \mu_i\right),\qquad(6)$$

where ρ_i is the density of component i, F is the Helmholtz energy functional, V_i^{ext} denotes the external potentials acting on component i, μ_i is the chemical potential of component i and $\mathbf{r}$ is the spatial coordinate. The external potential can be used to model e.g. fluid-solid interactions, and the shape of the external potential depends on the interactions to be modeled. In the following, similar to Stierle et al.,[41] we use square brackets to denote a functional dependence, and curly brackets to indicate a vector of all components in a mixture.

The grand canonical functional is minimum for a system at fixed temperature T, volume, and chemical potentials μ_i. The necessary conditions for a minimum of Eq. (6) are provided by the Euler-Lagrange equations,

$$\frac{\delta F\left[\{\rho_i\}\right]}{\delta\rho_j(\mathbf{r})} = \mu_j - V_j^{\mathrm{ext}}(\mathbf{r}),\qquad(7)$$

which is the system of equations solved in DFT. The thermodynamic description of the system under consideration is defined through a model for the Helmholtz energy functional capturing the ideal gas contribution and the contribution due to fluid-fluid interactions as well as expressions for the external potentials. We use a weighted density approximation to model the residual (intrinsic) Helmholtz energy functional, which accounts for fluid-fluid interactions

$$\beta F^{\mathrm{res}}\left[\{\rho_i(\mathbf{r})\}\right] = \int \mathrm{d}\mathbf{r}\,\Phi^{\mathrm{res}}\left(\{n_\alpha(\mathbf{r})\}\right),\qquad(8)$$

where Φ^{res} is the reduced residual Helmholtz energy density, and $\alpha \in \{1, \cdots\}$ is an index of the relevant weighted densities. The Helmholtz energy functional is obtained as a sum of residual Helmholtz energy functional and the ideal gas contribution, as $F = F^{\mathrm{res}} + F^{\mathrm{ig}}$. The weighted densities are calculated via convolutions with the density profiles,

$$n_\alpha(\mathbf{r}) = \sum_i^{N_c}\int \mathrm{d}\mathbf{r}'\,\rho_i(\mathbf{r}')\,\omega_i^\alpha(\mathbf{r} - \mathbf{r}')$$
$$\equiv \sum_i^{N_c}\rho_i(\mathbf{r}) \circledast \omega_i^\alpha(\mathbf{r}) = \sum_i^{N_c}n_{\alpha,i}(\mathbf{r}),\qquad(9)$$

where $\circledast$ denotes the convolution, ω_i^α is weight function α of component i, and N_c is the total number of components. The component-wise weighted densities are

$$n_{\alpha,i}(\mathbf{r}) = \rho_i(\mathbf{r}) \circledast \omega_i^\alpha(\mathbf{r}).\qquad(10)$$

The reduced, residual Helmholtz energy density of the DFT is modeled as

$$\Phi^{\mathrm{res}} = \Phi^{\mathrm{hs}} + \Phi^{\mathrm{nad}} + \Phi^{\mathrm{disp}}.\qquad(11)$$

Here, Φ^{hs} is the hard-sphere contribution, Φ^{nad} corrects for non-additivity in the hard-sphere contribution of mixtures, and Φ^{disp} is the contribution from dispersion interactions. In the following, we will explain how each of these terms are modeled.

B. The Hard-Sphere Contribution - Fundamental Measure Theory

We use fundamental measure theory (FMT) for the hard-sphere contribution of the Helmholtz energy functional. The weight functions used in Eq. (9) are

$$\omega_i^0(\mathbf{r}) = \frac{1}{4\pi R_i^2}\delta(R_i - |\mathbf{r}|), \tag{12a}$$

$$\omega_i^1(\mathbf{r}) = \frac{1}{4\pi R_i}\delta(R_i - |\mathbf{r}|), \tag{12b}$$

$$\omega_i^2(\mathbf{r}) = \delta(R_i - |\mathbf{r}|), \tag{12c}$$

$$\omega_i^3(\mathbf{r}) = \Theta(R_i - |\mathbf{r}|), \tag{12d}$$

$$\boldsymbol{\omega}_i^{\mathrm{V1}}(\mathbf{r}) = \frac{1}{4\pi R_i}\frac{\mathbf{r}}{|\mathbf{r}|}\delta(R_i - |\mathbf{r}|), \tag{12e}$$

$$\boldsymbol{\omega}_i^{\mathrm{V2}}(\mathbf{r}) = \frac{\mathbf{r}}{|\mathbf{r}|}\delta(R_i - |\mathbf{r}|), \tag{12f}$$

with the Heaviside step function Θ and the Dirac delta function δ. The hard-sphere radius of component i is

$$R_i = \frac{1}{2}\int_0^{\sigma_{ii,\mathrm{eff}}} \mathrm{d}r\left(1 - \exp\!\left(-\beta u_{ii}(r)\right)\right), \tag{13}$$

which depends on temperature. Furthermore, $\sigma_{ij,\mathrm{eff}}$ is defined by

$$u_{ij}(\sigma_{ij,\mathrm{eff}}, \beta) = 0. \tag{14}$$

FMT for hard-sphere mixtures was developed by Rosenfeld.[42] The name *fundamental measure* relates to the fundamental geometric measures of a sphere (volume, surface area, mean radius of curvature and the Euler characteristic). In this work, we use the White Bear version of FMT,[43] which reduces to the Boublík-Mansoori-Carnahan-Starling-Leland[44,45] EoS in homogeneous systems. The reduced Helmholtz energy density of the White Bear functional is

$$\Phi^{\mathrm{hs}} = -n_0\ln(1 - n_3) + \frac{n_1 n_2 - \mathbf{n}_1 \cdot \mathbf{n}_2}{1 - n_3}$$
$$+ \left(n_2^3 - 3n_2\mathbf{n}_2\cdot\mathbf{n}_2\right)\frac{n_3 + (1 - n_3)^2\ln(1 - n_3)}{36\pi n_3^2(1 - n_3)^2}. \tag{15}$$

The functional derivative on the left-hand-side of Eq. (7) can be calculated as

$$\frac{\delta\beta F^{\mathrm{hs}}[\{\rho_i\}]}{\delta\rho_j(\mathbf{r})} = \int \mathrm{d}\mathbf{r}\sum_\alpha \frac{\partial\Phi^{\mathrm{hs}}}{\partial n_\alpha(\mathbf{r}')}\cdot\frac{\delta n_\alpha(\mathbf{r}')}{\delta\rho_j(\mathbf{r})}. \tag{16}$$

Furthermore, it can be shown that[41]

$$\frac{\delta n_\alpha(\mathbf{r}')}{\delta\rho_j(\mathbf{r})} = \omega_j^\alpha(\mathbf{r} - \mathbf{r}'), \tag{17a}$$

$$\frac{\delta\mathbf{n}_\alpha(\mathbf{r}')}{\delta\rho_j(\mathbf{r})} = -\boldsymbol{\omega}_j^\alpha(\mathbf{r} - \mathbf{r}'), \tag{17b}$$

leading to

$$\frac{\delta\beta F^{\mathrm{hs}}[\{\rho_i\}]}{\delta\rho_j(\mathbf{r})} = \sum_{\alpha=0}^3 \frac{\partial\Phi^{\mathrm{hs}}}{\partial n_\alpha}\circledast\omega_j^\alpha - \sum_{\alpha=\mathrm{V1}}^{\mathrm{V2}} \frac{\partial\Phi^{\mathrm{hs}}}{\partial\mathbf{n}_\alpha}\circledast\boldsymbol{\omega}_j^\alpha, \tag{18}$$

which represents a convolution of the derivative of the reduced Helmholtz density Φ^{hs} with the weight functions ω_j^α from Eq. (12). Moreover, the derivatives of the reduced Helmholtz energy density with respect to the weighted densities are also functions of the weighted densities, which in turn come from convolution integrals (see Eq. (9)). Further details on the numerical calculation of these convolutions are provided in Sec. III.

C. The Non-additive Correction

Leonard, Barker, and Henderson laid the foundation for the perturbation theory of mixtures[38] in 1970. In a seminal paper, they derived a perturbation theory for mixtures from three different references: 1) a pure component hard-sphere fluid, 2) an additive hard-sphere mixture, and 3) a non-additive hard-sphere mixture. Since there is no established FMT for non-additive hard-sphere mixtures, we use an additive hard-sphere mixture as the reference. We showed in previous work that this yields nearly as accurate results as using a non-additive reference.[39]

The definition of an additive hard-sphere mixture is that the repulsive distance d_{ij} of any cross interaction equals the mean of the pure-fluid diameters, i.e., $d_{ij} = (d_i + d_j)/2$, where indices i and j refer to the two hard-sphere fluids, $d_i = \delta_{ii}$, and

$$\delta_{ij} = \int_0^{\sigma_{ij,\mathrm{eff}}} \mathrm{d}r\left(1 - \exp\!\left(-\beta u_{ij}(r)\right)\right). \tag{19}$$

The quantity δ_{ij} is often referred to as the effective hard-sphere diameter or the Barker–Henderson diameter. The origin of non-additivity stems from the combination rules of the molecular interaction potentials, Eqs. (4a)–(4d), where the interaction parameter l_{ij} for σ_{ij} is the main source of non-additivity.

The additional contribution to the reduced specific Helmholtz energy (a) that must be included to (approximately) account for non-additivity is

$$a^{\mathrm{nad}} = -\frac{2\pi}{\rho}\sum_i^{N_\mathrm{c}}\sum_j^{N_\mathrm{c}} \rho_i\rho_j d_{ij}^2 g_{\mathrm{mix,c}}^{ij}(d_{ij} - \delta_{ij}), \tag{20}$$

where ρ is the overall density and $g_{\mathrm{mix,c}}$ (subscript 'c') is the value of the radial distribution function of the additive hard-sphere mixture at contact. This contribution is zero when $d_{ij} = \delta_{ij}$. Leonard *et al.*[38] argued that the additional contribution from Eq. (20) is small, but they did not investigate the influence of this contribution on thermodynamic properties. In a recent work, we showed that it should be included to accurately reproduce the properties of non-additive mixtures,[39] and it has a particularly

large influence on the prediction of phase equilibria for hydrogen-helium and the deuterium-helium mixtures.[26]

To describe the radial distribution function at contact for inhomogeneous systems, we use the formulation proposed by Yu and Wu[46] for association, namely

$$g_{\text{mix,c}}^{ij}\left(\{n_\alpha\left(\mathbf{r}\right)\}\right) = \frac{1}{1-n_3} + \frac{d_i d_j}{d_i + d_j} \frac{\xi n_2}{2\left(1-n_3\right)^2} + \left(\frac{d_i d_j}{d_i + d_j}\right)^2 \frac{\xi^2 n_2^2}{18\left(1-n_3\right)^3}, \quad (21)$$

with $\xi = 1 - \mathbf{n}_2 \cdot \mathbf{n}_2 / n_2^2$. For the densities in Eq. (20), we use the FMT weighted densities $n_{0,i}$ scaled with $\xi_i = 1 - \mathbf{n}_{2,i} \cdot \mathbf{n}_{2,i} / n_{2,i}^2$, leading to

$$\Phi^{\text{nad}} = \\ -2\pi \sum_i^{N_c} \sum_j^{N_c} n_{0,i} \xi_i n_{0,j} \xi_j d_{ij}^2 g_{\text{mix,c}}^{ij}\left(\{n_\alpha(\mathbf{r})\}\right)\left(d_{ij} - \delta_{ij}\right). \quad (22)$$

D. The Dispersion Contribution

The structure of the dispersion contribution of the Feynman–Hibbs corrected Mie potentials to the Helmholtz energy functional is based on the development of Sauer and Gross,[35]

$$\Phi^{\text{disp}}\left(\{n_i^{\text{disp}}\left(\mathbf{r}\right)\}\right) \equiv n^{\text{disp}}\left(\mathbf{r}\right) a^{\text{disp}}(\{n_i^{\text{disp}}\left(\mathbf{r}\right)\}), \quad (23)$$

with the reduced specific Helmholtz energy a^{disp} from the SAFT-VRQ Mie EoS to be consistent with the bulk EoS.

The weighted densities $n_i^{\text{disp}}\left(\mathbf{r}\right)$ of the dispersion contribution (with $n^{\text{disp}}\left(\mathbf{r}\right) = \sum_i n_i^{\text{disp}}\left(\mathbf{r}\right)$) can be calculated from Eqs. (9) and (10) with the weight function for the dispersion contribution of component i, defined by

$$\omega_i^{\text{disp}}\left(\mathbf{r}\right) = \frac{\Theta\left(2\psi R_i - |\mathbf{r}|\right)}{\frac{4\pi}{3}\left(2\psi R_i\right)^3}, \quad (24)$$

using the model parameter $\psi = 1.3862$ proposed by Sauer and Gross,[35] which was shown to reproduce the surface tension of n-alkanes when combining DFT with the PC-SAFT EoS.

III. NUMERICAL METHODS

This section will present the main details of the numerical solution of the DFT and the molecular simulations.

A. Convolution in Planar Geometries

The convolution integrals described in Eqs. (9), (10) and (18) can be efficiently computed in Fourier space by using available fast Fourier transform (FFT) algorithms described by Knepley et al.,[47] Stierle et al.,[41,48] and references therein. The complexity of the transforms can be reduced by assuming periodic and even/odd symmetric profiles that are convolved with the weight functions from Eqs. (12) and (24). An advantage of this approach is that it avoids the need of 'buffer-zones' outside of the computational domain,[41] and simplifies the grid. Sec. 1 of the Supplementary Information (SI) gives an introduction to how the FFT can be split into sine and cosine transforms, and how they apply to even and odd functions. This will be exploited in the following. Definitions for the cosine and sine transform as well as the corresponding inverse transforms are also found in Sec. 1 of the SI.

The weight functions in Eqs. (12) and (24) are analytically transformed to Fourier space,[41] and the functions are defined in Appendix A. The circumflex (ˆ) above the functions refers to the Fourier transforms of the respective quantity.

The Fourier transforms presented in the following can be efficiently computed using fast discrete sine and cosine transform algorithms. The grid used in Fourier space for the planar geometries is defined and illustrated in Appendix B.

1. Convolution with Scalar-Valued Weight Functions

The densities, the scalar-valued weighted densities, the scalar-valued partial derivatives of the Helmholtz energy densities from FMT and the dispersion functional are all even functions in a planar geometry. They can therefore be transformed into Fourier space using a cosine transform according to

$$\hat{\rho}_i(k_z) \equiv \mathcal{COS}\left[\rho_i(z)\right], \quad (25)$$

where k_z is the Fourier space coordinate. The convolution that defines the scalar-valued weighted densities can be computed as

$$n_{\alpha,i}(z) = \mathcal{COS}^{-1}\left[\hat{\rho}_i(k_z)\hat{\omega}_i^\alpha(k_z)\right], \quad (26)$$

with the inverse cosine transform $\mathcal{COS}^{-1}$.

The scalar-valued partial derivatives of the Helmholtz energy density, Eq. (18), are also even functions. They are transformed to Fourier space according to

$$\frac{\hat{\partial\Phi}}{\partial n_\alpha}(k_z) \equiv \mathcal{COS}\left[\frac{\partial\Phi}{\partial n_\alpha}(z)\right]. \quad (27)$$

The convolution of the (even) scalar-valued partial derivatives of the Helmholtz energy and the (even) scalar weight functions, defined in Eqs. (12) and (24), or in Fourier space in Eqs. (A1) and (A2), can be computed by

$$\frac{\partial\Phi}{\partial n_\alpha}(z) \circledast \omega_j^\alpha(z) = \mathcal{COS}^{-1}\left[\frac{\hat{\partial\Phi}}{\partial n_\alpha}(k_z)\hat{\omega}_j^\alpha(k_z)\right]. \quad (28)$$

2. Convolution with Vector-Valued Weight Functions

Because the vector-valued weight functions from FMT are odd functions, the vector-valued weighted densities, $\mathbf{n}_{\alpha,i}$, are transformed back from Fourier space using the sine transform via

$$\mathbf{n}_{\alpha,i}(z) = \imath \, \mathcal{SIN}^{-1} \left[\hat{\rho}_i(k_z) \hat{\boldsymbol{\omega}}_i^\alpha(k_z) \right], \qquad (29)$$

since the argument of the inverse sine transform is scalar-valued (odd).

The vector-valued partial derivatives of the Helmholtz energy density from FMT, Eq. (16), are odd functions. They are transformed to Fourier space using the sine transform,

$$\frac{\partial \hat{\Phi}}{\partial \mathbf{n}_\alpha}(k_z) \equiv -\imath \, \mathcal{SIN} \left[\frac{\partial \Phi}{\partial \mathbf{n}_\alpha}(z) \right]. \qquad (30)$$

Although the imaginary unit, $\imath \equiv \sqrt{-1}$, appears in Eqs. (29) and (30), the use of complex numbers can be avoided completely by adjusting the sign of the convolution results, noting the imaginary unit appears quadratically ($\imath^2 = -1$). The convolution of the (odd) vector-valued derivatives of the Helmholtz energy density and the (odd) vector-valued weight functions is

$$\frac{\partial \Phi}{\partial \mathbf{n}_\alpha}(z) \circledast \boldsymbol{\omega}_j^\alpha(z) = \mathcal{COS}^{-1} \left[\frac{\partial \hat{\Phi}}{\partial \mathbf{n}_\alpha}(k_z) \cdot \hat{\boldsymbol{\omega}}_j^\alpha(k_z) \right], \quad (31)$$

where the argument of the inverse cosine transform is scalar-valued (due to the scalar product and because the product of two odd functions yields an even function).

B. Iterative Solution for Density Profiles

The equilibrium density profiles are obtained from DFT by solving Eq. (7). By substituting the exactly known ideal gas contribution for the chemical potential $\beta\mu_j^{\mathrm{ig,b}} = \ln(\rho_j^{\mathrm{b}} \Lambda_j^3)$ and the functional derivative $\frac{\delta \beta F^{\mathrm{ig}}}{\delta \rho_j} = \ln(\rho_j(\mathbf{r}) \Lambda_j^3)$, the following fixed-point equation is obtained

$$\rho_j(z) = \rho_j^{\mathrm{b}} \exp \left(\beta\mu_j^{\mathrm{res,b}} - \beta V_j^{\mathrm{ext}}(z) - \frac{\delta \beta F^{\mathrm{res}}[\{\rho_i\}]}{\delta \rho_j(z)} \right). \qquad (32)$$

The fixed-point equations can be solved by a combination of simple Picard iterations and/or Anderson mixing,[49,50] also called Pulay mixing[51,52] or direct inversion in the iterative subspace (DIIS).[53] We refer the interested reader to the work of Mairhofer and Gross[54] for more details and comparison of different methods for solving Eq. (32). The fixed-point iterations can be stabilized by introducing additional constraints, e.g., for the total number of molecules in the system. We have included more details on this in Appendix C.

C. Calculating Surface Tensions

The surface tensions are calculated for planar interfaces in one-dimensional Cartesian coordinates for pure fluids and mixtures. The initial condition partial density profiles $\rho_i^{\mathrm{IC}}(z)$ are generated using a hyperbolic tangent function proposed by Mairhofer et al.,[55] as

$$\rho_i^{\mathrm{IC}}(z) = \frac{1}{2} \left(\rho_i^{\ell,\mathrm{b}} + \rho_i^{\mathrm{v,b}} \right)$$
$$+ \frac{1}{2} \left(\rho_i^{\ell,\mathrm{b}} - \rho_i^{\mathrm{v,b}} \right) \tanh \left(\frac{z}{d_i} \left(2.4728 - 2.3625 \frac{T}{T^{\mathrm{c}}} \right) \right). \qquad (33)$$

Here, T^{c} refers to the critical temperature calculated from the liquid composition. The bulk properties of liquid (ℓ) and vapor (v) are calculated from phase equilibrium calculations with knowledge of the temperature for pure fluids and an additional specification for the binary systems. This additional specification is either the liquid composition or the vapor phase densities.

For the simulation of the planar interfaces the external potentials in Eqs. (6), (7) and (32) are set to zero for all components, $V_j^{\mathrm{ext}}(\mathbf{r}) = 0 \, \forall \, j$.

Using the equilibrium density profiles, the surface tension γ is calculated from the reduced Helmholtz energy density Φ, the chemical potentials μ_i, and the bulk pressure p^{b}, all three properties comprising ideal gas plus residual contributions, by evaluating the following integral, which is only non-zero in the interface region

$$\gamma = \int_{-\infty}^\infty \mathrm{d}z \left(k_{\mathrm{B}} T \Phi(\{\rho_i(z)\}) - \sum_i^{N_{\mathrm{c}}} \mu_i \rho_i(z) + p^{\mathrm{b}} \right), \qquad (34)$$

with the z-direction being perpendicular to the interface.

D. The Radial Distribution Function determined from DFT and from Molecular Dynamics Simulations

Within the DFT formalism, the radial distribution functions and (self-) solvation free energies can be obtained via Percus' test particle theory.[56,57] In this method, the intermolecular pair potential (the Feynman–Hibbs corrected Mie potential) is used as the external potential, $V_i^{\mathrm{ext}}(\mathbf{r})$ in Eq. (6), at the origin of the system.

Solving the DFT, the resulting equilibrium density profile for a homogeneous fluid in a one-dimensional spherical coordinate system can be used to calculate the radial distribution function,

$$g(r) = \frac{\rho(r)}{\rho^{\mathrm{b}}}, \qquad (35)$$

where $\rho(r)$ is the density profile from the DFT and ρ^{b} is the value from the EoS for a homogeneous system. For binary mixtures, the same methodology is applied but two DFT computations are required: one calculation for the

intermolecular pair potential of each component, which acts as an external potential. We refer to the work by Eller *et al.*[57] and the SI of this work for further details about these calculations.

The radial distribution function from DFT can be compared to results from molecular dynamics simulations (MD). For this purpose, we have carried out MD simulations using the open-source code LAMMPS[58] in the NVT ensemble with a time step of $\Delta t = 1.0\,\text{fs}$ using a Nosé-Hoover thermostat and a damping time of $t_{\text{damp}} = 100\,\text{fs}$. The Feynman–Hibbs corrected Mie potentials for all interaction pairs were provided as energy and force tables (5000 values, equidistant between $r_{\text{min}} = 0.1\,\text{Å}$ and $r_{\text{max}} = 12.0\,\text{Å}$) evaluated at the simulation temperature. The cut-off distance was the maximum distance of the tabulated potential ($r_{\text{c}} = 12.0\,\text{Å}$) and the same cut-off distance was used for all intermolecular potentials.

The thermodynamic conditions for the simulations were generated as follows. The SAFT-VRQ Mie EoS was used to calculate the bubble point for a given temperature and mixture composition. Next, the pressure was increased to ensure a stable liquid phase. For the resulting temperature, pressure, and composition, the density was computed from which – for a fixed number of Mie interaction sites, $N = 4000$ – the length of the cubic simulation box was determined. The Mie sites were randomly placed in the simulation box. An energy minimization was conducted prior to an equilibration ($t_{\text{equil}} = 0.1\,\text{ns}$) and subsequent production ($t_{\text{prod}} = 1.0\,\text{ns}$). During the production phase, the radial distribution function was sampled (500 bins in $r = [0, r_c]$, every 100-th step) and the running average stored. LAMMPS input files, energy and force tables, Jupyter notebooks and plots for the investigated binary mixture's radial distribution functions are available in the SI.

IV. RESULTS AND DISCUSSION

Neon, deuterium, hydrogen, helium and their mixtures display vapor-liquid phase equilibria at temperatures below 60 K, where other substances form solids. At these conditions, the influence of quantum effects can be significant.

Both, hydrogen and deuterium have two isomeric forms, referred to as spin isomers. The two nuclear spins of the protons of ortho-hydrogen are aligned parallel, while for para-hydrogen, they are aligned antiparallel. The equilibrium ratio of the spin isomers at high temperatures is referred to as normal-hydrogen, which is a mixture of 75 % ortho-hydrogen and 25 % para-hydrogen. Similarly, the ratio of ortho-deuterium to para-deuterium is 2:1 for 'normal'-deuterium. In the following, we will restrict the discussion to normal-hydrogen, normal-deuterium and para-hydrogen. Normal-hydrogen and normal-deuterium will in this work be treated as pure fluids and referred to as hydrogen and deuterium.

For hydrogen, para-hydrogen, helium and neon, we have

TABLE I: Mie potential parameters used with first-order Feynman–Hibbs corrections

Substance	$\sigma/\text{Å}$	$(\epsilon/k_{\text{B}})/\text{K}$	λ_{a}	λ_{r}
Helium	2.7443	5.4195	6	9
Hydrogen	3.0243	26.706	6	9
Para-hydrogen	3.0235	26.5860	6	9
Deuterium	3.0087	39.2388	7	11
Neon	2.7778	37.501	6	13

used the parameters of the Feynman-Hibbs corrected Mie potentials from previous work.[25] For deuterium however, the parameters have been improved to achieve more accurate liquid-phase densities at low temperatures, with small influence on other thermodynamic properties. But, even with the new parameters the predictions for the liquid densities of deuterium deviate from the experimental values below the normal boiling point. More details on the regression of new parameters for deuterium are available in the SI.

The parameters of the pure-component interaction potentials used in this work are listed in Tab. I. For mixtures, the same combination rules as in our previous work were used.[26]

All of the results presented in this work have been reproduced using both, the open-source FeOs framework[59,60] and the open-source Thermopack framework.[61,62] This has served as a consistency check for the implementation.

A. The Radial Distribution Function of Feynman-Hibbs corrected Mie fluids

To gain confidence in predicting interfacial properties using DFT, we first assess how well DFT is able to predict the fluid structure in bulk phases. We compare the radial distribution functions (RDFs) calculated from DFT to results from molecular simulations. Details about these calculations can be found in Sec. III D and in the SI.

The liquid-phase states for the single-component fluids are listed in Tab. II. The states are found for temperatures at approximately 0.8 of the critical temperature ($T \approx 0.8T^{\text{c}}$) and densities that are slightly increased from the saturation density at this temperature. With these states as input, we calculated the RDFs of helium, hydrogen, deuterium and neon represented by Feynman-Hibbs corrected Mie potentials. Fig. 2 shows an excellent agreement between predictions from DFT and results from MD simulations. This suggests that the DFT functional is suitable for inhomogeneous systems with pronounced local density correlations.

A similar comparison that extends these findings to mixtures can be found in the SI. For mixtures, we find that it is key to include the non-additive contribution described in Sec. II C to be able to represent the RDF of mixtures that have significant non-additivity. For in-

(a) Helium
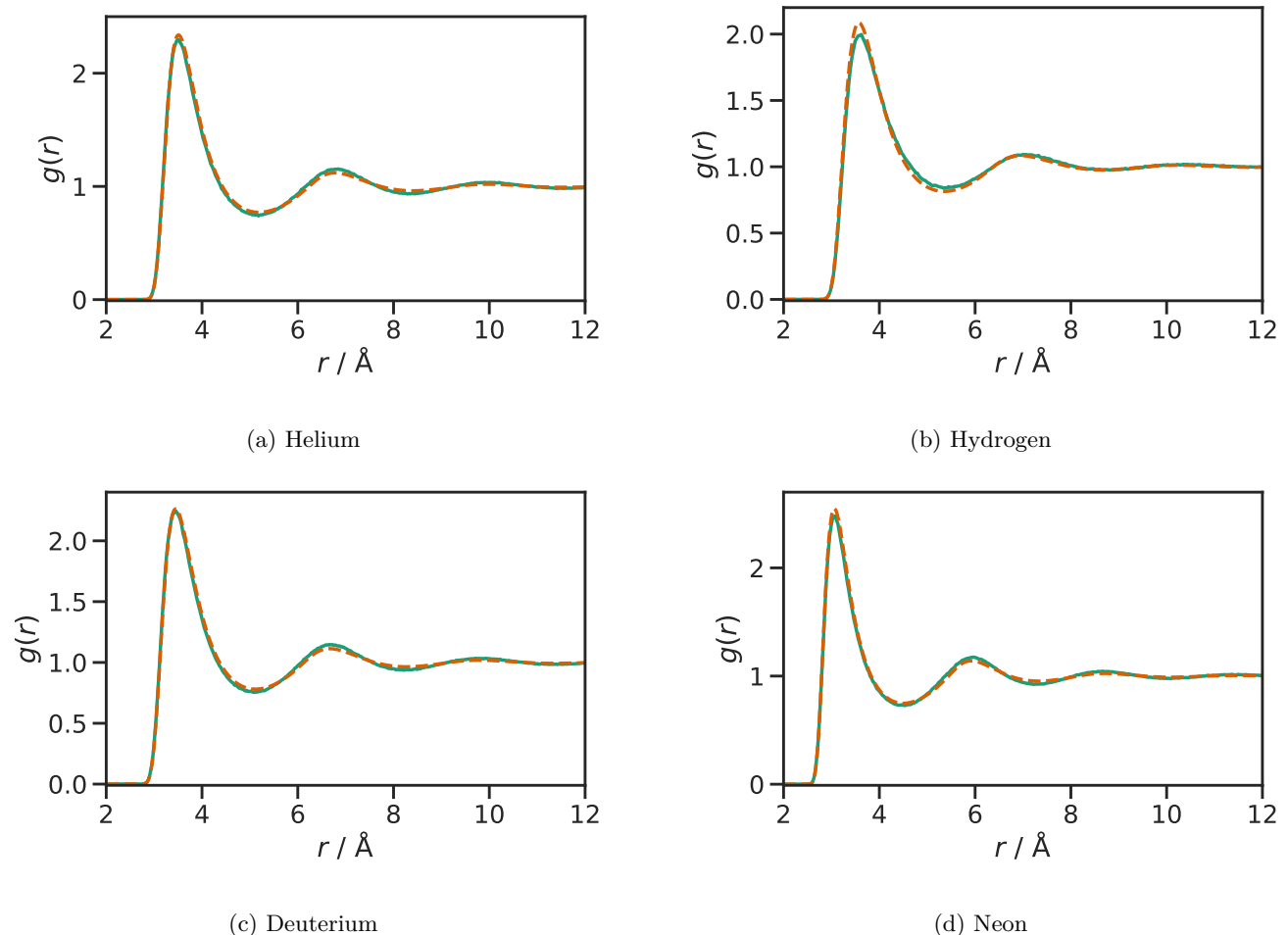
(b) Hydrogen

(c) Deuterium

(d) Neon

FIG. 2: Radial distribution functions of pure fluids from DFT (orange, dashed) and MD simulations (green, solid).

TABLE II: Pure fluid states for calculating RDF.

Substance	T/K	$\rho/(\mathrm{kg/m}^3)$
Helium	4.0	137.5
Hydrogen	27.5	61.5
Deuterium	30.0	145.0
Neon	35.0	1050.0

stance, the local stucture arbound helium atoms in a helium-deuterium mixture at 30 K and 50 bar from DFT is only in agreement with results from molecular simulation if the additional non-additive contribution from Sec. II C is included in the Helmholtz energy functional.

B. Surface Tensions of Pure Fluids

Mulero *et al.*[63] correlated the surface tensions of several pure-component fluids to experimental data. They presented empirical correlations formulated as polynomials in reduced temperature (T/T^{c}). The correlations agree well with the experimental data for neon and deuterium. For para-hydrogen however, the agreement is poor above 20 K. A new correlation for the surface tension of para-hydrogen has therefore been developed, where details can be found in the SI. For hydrogen, the correlation by Mulero *et al.* is in good agreement with available experimental data for most of the temperature range, but it displays a nonphysical kink close to the critical temperature. A new correlation without this kink has been developed for hydrogen, where details can be found in the SI. The critical temperatures used in this work for evaluation of the correlations are tabulated in Tab. III. In the following, we assess the accuracy of the DFT by comparing to the empirical correlations and to experimental data.

Fig. 3 compares the surface tensions from DFT to correlations and available experimental data for hydrogen, para-hydrogen (the hydrogen isomer stable at low temperatures), deuterium, and neon. Hydrogen, para-hydrogen and deuterium, shown in Fig. 3a, Fig. 3b and Fig. 3c respectively, show good agreement with the experiments, but with increasing deviation as the temperature

(a) Hydrogen
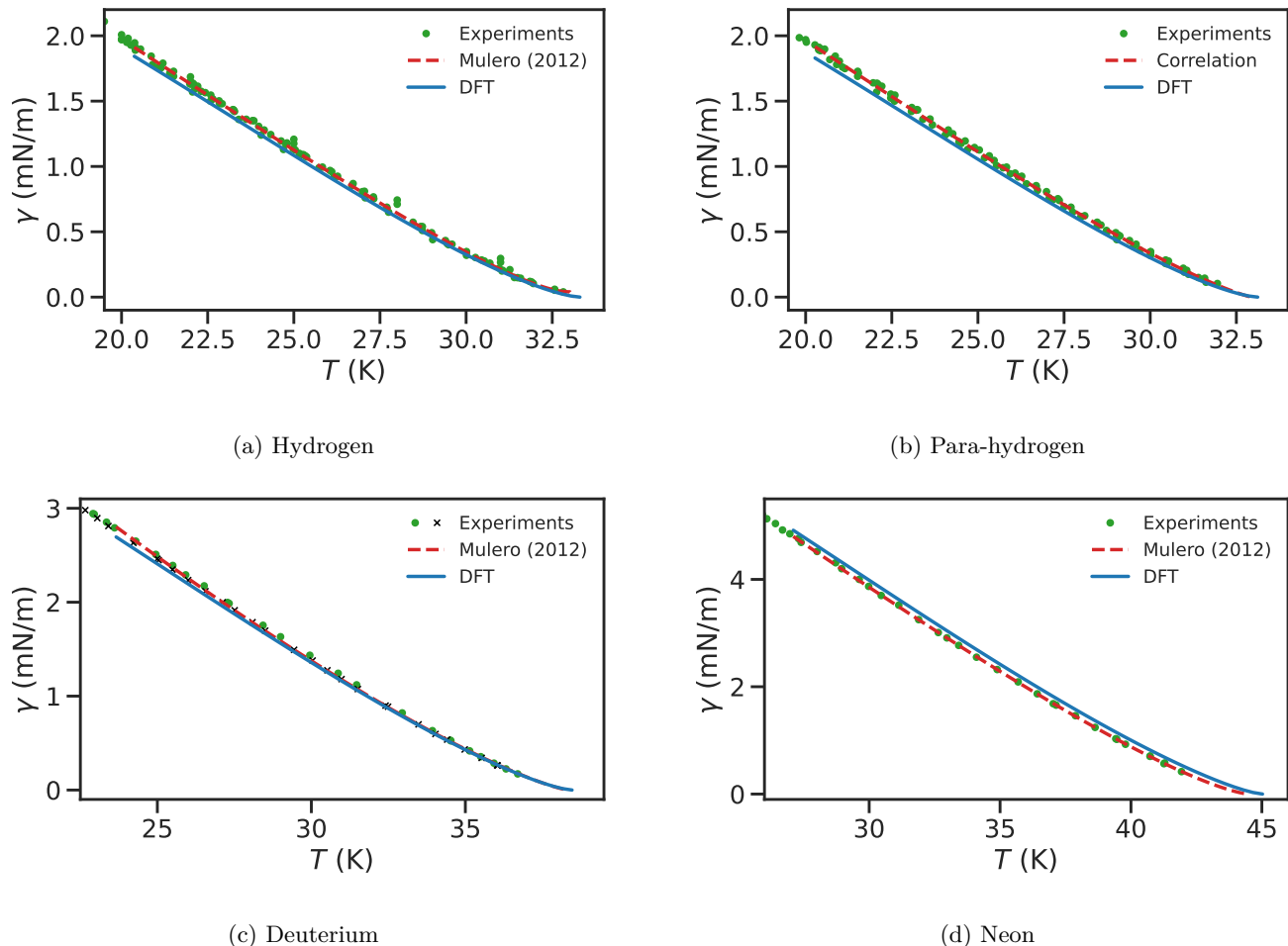
(b) Para-hydrogen

(c) Deuterium

(d) Neon

FIG. 3: Surface tension calculated using DFT is compared to experimental data and correlations. A new correlation (see SI) is used for para-hydrogen, while the correlations of Mulero et al.[63] are used for the other fluids. For deuterium, the experimental data of ortho-deuterium is included in the diagram (crosses).

TABLE III: Critical and normal boiling point temperatures (NBT) of the quantum fluids.[64–66]

Substance	$T^{\mathrm{c}}/\mathrm{K}$	$T^{\mathrm{NBT}}/\mathrm{K}$
Hydrogen	33.145	20.369
Para-hydrogen	32.938	20.271
Deuterium	38.34	23.661
Neon	44.4918	27.104

decreases. This is consistent with the modest under-prediction of the density of the saturated liquid by the Feynman-Hibbs corrected Mie potential and the EoS at these conditions. In Fig. 3c we include the experimental data of ortho-deuterium in the diagram for deuterium. The data of ortho-deuterium deviate to a small extent from the data of normal-deuterium.

For neon, shown in Fig. 3d, the relative deviations between DFT-results from experimental data increases

with temperature. The most likely reason for these deviations are small errors of the EoS already observed for bulk properties, in particular a deviation in the critical temperature.

In the temperature-range from normal boiling point to 95 % of the critical temperature ($T^{\mathrm{boil}} \leq T \leq 0.95\ T^{\mathrm{c}}$), the DFT predicts surface tensions for neon, hydrogen, para-hydrogen, and deuterium with average deviations from experimental results of 7.5 %, 4.4 %, 6.7 %, and 1.8 %, respectively. These errors have been estimated with an equidistant temperature grid (100 points). No parameters of the DFT-model were adjusted to interfacial properties, which is why we refer to the DFT results as predictions.

From Fig. 3 we see that the predictions for all fluids are in good agreement with the experimental data. Also the availability of experimental data is excellent for hydrogen and para-hydrogen. For deuterium, only one good source of experimental data has been found with temperatures ranging from $20.57\,\mathrm{K}$ to $36.7\,\mathrm{K}$.[67] One reference with data in a similar range is also reported for ortho-

deuterium.[68] The availability of data for neon is fairly good, but only two data sets with measurements up to 41.93 K are available.[69,70]

C. Surface Tensions of Mixtures

There are few published measurements of the surface tensions of mixtures of helium, hydrogen, deuterium and neon. To the best of our ability, we could only find data of four mixtures, which will be discussed in the following. For all of these mixtures, the surface tensions were measured with the capillary-rise method.

Blagoi and Pashkov[74] measured four isotherms ($T \in \{24.59, 26.33, 27.15, 29.00\}$ K) of the hydrogen-neon mixture. The measured pressures range from 1.91 atm to 5.90 atm, and the surface tension was shown to decrease rapidly with increasing hydrogen concentration. Fig. 4d compares predictions from DFT to the experimental data with composition ranging from pure neon to the triple point composition. An almost linear decrease in surface tension with increasing hydrogen content is thereby observed. The experimental data appears to follow a more convex composition-dependence. All of the predictions fall within 10 % of the experimental data, with a mean absolute deviation (MAD) of 7.5 %.

Grigorev and Rudenko[71] measured the surface tensions of eight hydrogen-deuterium mixtures with deuterium mole fractions from 7.2 % to 82.3 %. The measured temperatures were in the range 16.44 K to 20.46 K. In Fig. 4a, two isotherms (18.88 ± 0.2 K and 20.44 ± 0.2 K) have been extracted from the experimental data. The surface tensions from DFT show the same trend as the experimental values. However, since the measured temperatures are all below the normal boiling point of deuterium, the EoS predictions for the liquid-phase density of deuterium deviate from the experimental values. The error in the liquid densities predicted by the model result in a deviation between DFT and experiments for the surface tension, which is especially large in the limit of pure deuterium. The MAD of the hydrogen-deuterium system was found to be 5.4 %.

In a series of articles, Paine and Seidel[72,73,75] reported measurements of the adsorption energy of helium on the surface of liquid hydrogen and of liquid deuterium. The spin-isomer composition of hydrogen and deuterium were equilibrated at low temperatures (20 K) using a magnetic catalyst. The equilibrium composition is then nearly pure para-hydrogen, while deuterium is converted to almost pure ortho-deuterium.

The dependence of the surface energy of liquid hydrogen on the helium gas density was measured using the capillary-rise technique, and the experiments were equilibrated for 10 min until mechanical and thermal equilibrium was established in the experimental cell. The bulk liquid phase was, however, not in compositional (chemical) equilibrium. Paine and Seidel estimated the diffusion coefficient of helium in hydrogen to be 0.1 μm s^{-1} to 1 μm s^{-1}.

Despite of being out of equilibrium with net transport of helium across the interface, the diffusion lengths for the equilibration time are orders of magnitude larger than the size of the relevant interface region. Hence, it is reasonable to assume the gradient in chemical potentials to be zero, i.e., assume chemical equilibrium in spatial coordinate across the nanosized interfacial region considered in the DFT calculations. Because the properties of ortho-deuterium and para-deuterium are very similar, we used the parametrization for normal-deuterium to describe ortho-deuterium. The interaction between para-hydrogen and helium was set to $k_{ij} = 0.08$ and $l_{ij} = -0.05$, the same as for hydrogen and helium.

The surface tension data of Paine and Seidel are measured as a function of the helium partial densities in the vapor phase.[72,73] To compare the experiments to predictions from DFT, the vapor-liquid equilibrium condition was solved to extract the specific component mass density of helium, $\rho_{\text{He}}^{(m)}$.

Four isotherms for helium with para-hydrogen, at $T \in \{15, 17, 19, 21\}$ K, are shown in Fig. 4b. The two isotherms with lowest temperature extrapolate well towards the pure fluid correlation (represented by a star-symbol in Fig. 4b). Extrapolating the isotherms at $T = 19$ K and $T = 21$ K, however, indicate too high values of the surface tensions for the mixtures. The DFT results deviate for pure para-hydrogen, an offset that remains for increased helium content, although the DFT shows the same trend as the experimental data. Overall, the MAD found for the helium-para-hydrogen mixture is 8.1 %.

Fig. 4c shows six isotherms for the helium-deuterium mixture ($T \in \{20, 21, 22, 23, 24, 26\}$ K). Predictions from the DFT are in good agreement with the experimental data, and the mixture-data agrees fairly well with the quasi-experimental correlation for pure liquid deuterium. The MAD was found to be 1.3 %.

V. CONCLUSION

Neon, deuterium, hydrogen, helium and their mixtures display vapor-liquid phase equilibria at temperatures below 60 K. At these conditions, other components form solids and the influence of quantum effects can be significant. We present a classical density functional theory (DFT) for these fluids that can be used to study interfacial properties at temperatures above 20 K.

The DFT is based on a third-order thermodynamic perturbation theory of Feynman–Hibbs quantum corrected Mie potentials called the SAFT-VRQ Mie EoS. White Bear fundamental measure theory is used to describe the additive hard-sphere mixture, and a new functional contribution has been developed to correct for non-additivity. The correction is incorporated into the DFT through a functional representation of the radial distribution function at contact. A weighted density approximation is used for the dispersion contribution.
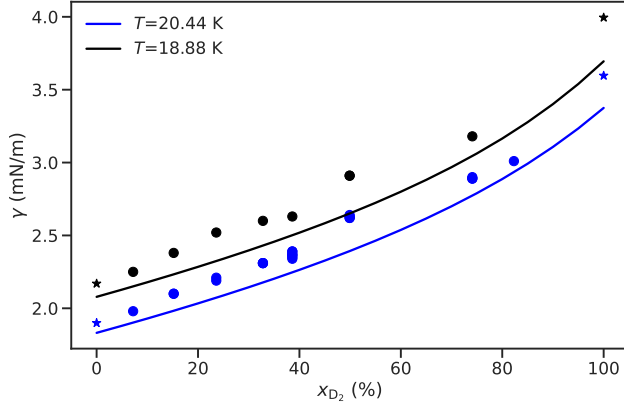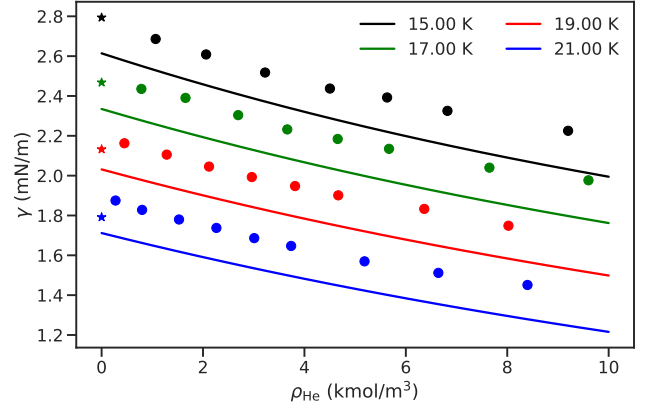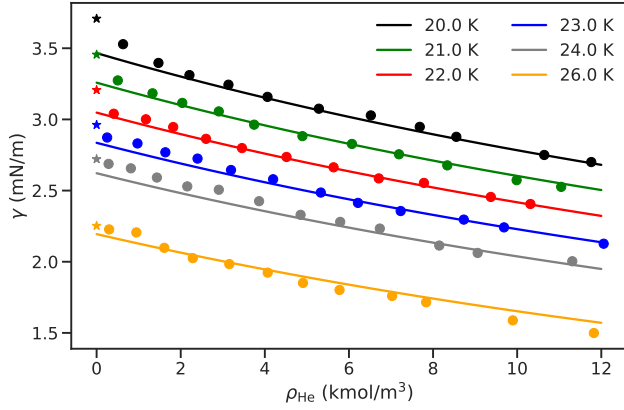
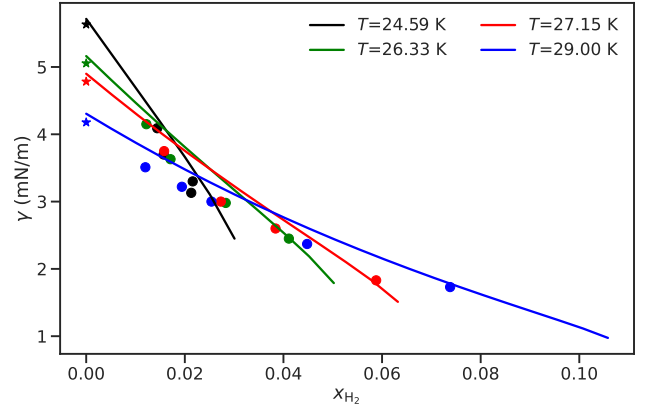The ability of the DFT to capture the pair-wise struc-

(a) Hydrogen-deuterium[71]

(b) Para-hydrogen-helium[72]

(c) Deuterium-helium[73]

(d) Hydrogen-neon[74]

FIG. 4: Isothermal surface tension calculated using DFT (solid lines) compared to experimental data (dots) and pure fluid values (asterisk) calculated form correlations. For para-hydrogen (4b) the new correlation is used otherwise the Mulero *et al.*[63] correlation is used.

ture of the quantum corrected Mie fluid in bulk phases was evaluated by computing the radial distribution function utilizing Percus' test particle theory. The radial distribution function from DFT was found to be in excellent agreement with results from molecular dynamic simulations performed with Feynman–Hibbs quantum corrected Mie potentials of both pure fluids and mixtures.

For ranges of temperature between the normal boiling point and 95 % of the critical temperature, the DFT yields surface tensions of neon, hydrogen, para-hydrogen, and deuterium with average deviations from experimental data of 7.9 %, 4.4 %, 6.7 %, and 1.8 %, respectively.

The surface tensions of hydrogen–deuterium, para-hydrogen–helium, deuterium–helium, and hydrogen–neon mixtures from experiments were reproduced within a mean absolute error of 5.4 %, 8.1 %, 1.3 %, and 7.5 %, respectively. The DFT model predicts the surface tension of fluids that exhibit strong quantum effects with excellent accuracy at temperatures above approximately 20 K.

The decreased accuracy of the model at lower temper-

atures ($T < 20$ K) comes from the inability of Feynman–Hibbs corrected Mie potentials to represent the thermodynamic properties of the real (bulk) fluids. We thus identify a need for developing new force fields for quantum fluids that are accurate, also below 20 K.

Although prediction of surface tensions was the primary focus of the present work, the presented DFT model can in the future be used to study confined fluids.[24] An interesting future application is to assess the performance of porous materials for storage and transport of hydrogen.

SUPPLEMENTARY MATERIAL

We refer to the online supplementary material for basic information on the efficient calculation of convolution integrals using the convolution theorem and the Fourier transform, plots showing how the modified SAFT-VRQ Mie EoS used in this work compares to the originally published EoS, a comparison of the radial distribution function calcu-

lated from DFT to results from MD simulations, and new correlations for the surface tension of normal-hydrogen and para-hydrogen. The supplementary material also contains a zip-file showing how to calculate the radial distribution functions of the quantum binary systems from MD and DFT.

AUTHOR DECLARATIONS

A. Conflict of Interest

The authors have no conflicts of interest to disclose.

DATA AVAILABILITY

The following data is provided in a zip-file as part of the supplementary information:

- LAMMPS input files for all binary systems (*lammps_inputs* folder)

- Jupyter notebook with a tutorial explaining how to generate LAMMPS tables and input files as well as how to conduct the DFT computations for radial distribution functions using FeO_s. (*walkthrough* folder)

- HTML file of the tutorial. (*walkthrough* folder)

- LAMMPS tables, input files and results for the tutorial. (*walkthrough* folder)

Appendix A: Analytically Transformed Weight Functions

The weight functions in Eqs. (12) and (24) can be analytically transformed to Fourier space[41]

$$\hat{\omega}_i^0(k_z) = j_0(2\pi R_i|k_z|), \tag{A1a}$$

$$\hat{\omega}_i^1(k_z) = R_i j_0(2\pi R_i|k_z|), \tag{A1b}$$

$$\hat{\omega}_i^2(k_z) = 4\pi R_i^2 j_0(2\pi R_i|k_z|), \tag{A1c}$$

$$\hat{\omega}_i^3(k_z) = \frac{4}{3}\pi R_i^3\big(j_0(2\pi R_i|k_z|) + j_2(2\pi R_i|k_z|)\big), \tag{A1d}$$

$$\hat{\omega}_i^{V1}(k_z) = \frac{-\imath k_z}{2R_i}\hat{\omega}_i^3(k_z), \tag{A1e}$$

$$\hat{\omega}_i^{V2}(k_z) = -\imath 2\pi k_z\hat{\omega}_i^3(k_z). \tag{A1f}$$

The Fourier transform of the dispersion weight is

$$\hat{\omega}_i^{disp}(k_z) = j_0(4\pi\psi R_i|k_z|) + j_2(4\pi\psi R_i|k_z|), \tag{A2}$$

where the spherical Bessel functions of the first kind of order zero and two are

$$j_0(x) = \frac{\sin(x)}{x}, \tag{A3a}$$

$$j_2(x) = \left(\frac{3}{x^2} - 1\right)\frac{\sin(x)}{x} - \frac{3\cos(x)}{x^2}. \tag{A3b}$$

Appendix B: Grid in Fourier Space in Planar Geometries

The sine and cosine transforms used in Sec. III A can be efficiently computed using fast discrete sine and cosine transform algorithms.

For the numerical grid depicted in Fig. 5, the appropriate algorithms are the discrete sine and cosine transform variant II ($\mathcal{DST}_{II}$ and $\mathcal{DCT}_{II}$, respectively) for the transformation to Fourier space and variant III for the transformation from Fourier back to real space ($\mathcal{DST}_{III}$ and $\mathcal{DCT}_{III}$). Fig. 5 illustrates how the $\mathcal{DST}_{II}$ and $\mathcal{DCT}_{II}$ assume periodic even/odd symmetric profiles.

The corresponding discrete k_z-grid can be obtained by discretizing the continuous cosine transform, using $z_j = (j + \frac{1}{2})\Delta z$ and $\mathfrak{f}(z_j) = \mathfrak{f}_j$, resulting in

$$\hat{\mathfrak{f}}(k_z) = 2\int_0^\infty dz\, \mathfrak{f}(z)\cos(2\pi z k_z)$$

$$\approx 2\sum_{j=0}^{N-1}\mathfrak{f}_j\cos\left(2\pi\left(j+\frac{1}{2}\right)\Delta z k_z\right), \tag{B1}$$

and comparing it to the discrete cosine transform defined in Eq. (7a) in the SI. Comparison of the arguments, $2\pi(j+\frac{1}{2})\Delta z k_z = \frac{\pi}{N}(j+\frac{1}{2})k$, leads to

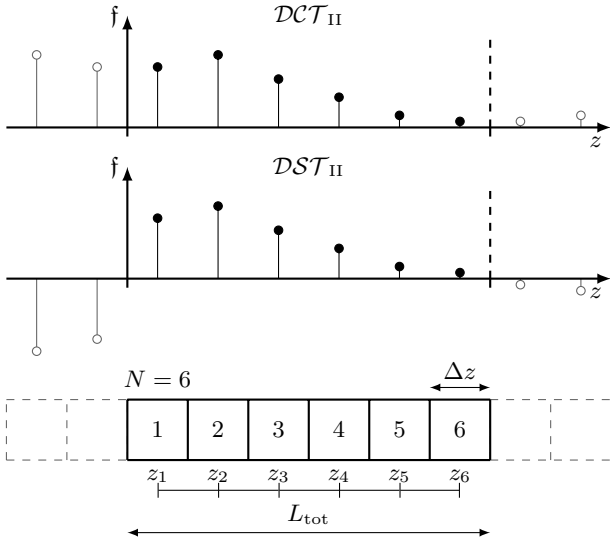$$k_z \equiv \frac{k}{2N\Delta z} = \frac{k}{2L_{tot}} \qquad \text{with } k = 0,\cdots,(N-1). \tag{B2}$$

FIG. 5: Schematic equidistant Cartesian grid with $N = 6$ grid points and grid spacing Δz. All profiles $\mathfrak{f}(z)$ to be transformed are computed on the domain L_{tot} and evaluated at the center of the grid cells z_i. The implicit even/odd continuation is visualized for the discrete cosine and sine transforms, $\mathcal{DCT}_{\text{II}}$ and $\mathcal{DST}_{\text{II}}$, respectively.

The '$2L_{\text{tot}}$' in the denominator of Eq. (B2) indicates that the domain length of the profiles to be transformed is actually the double of L_{tot}, and that the even or odd symmetries of the profile are exploited.
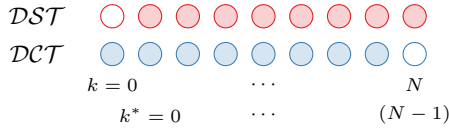

FIG. 6: Required shift of indices to match $\mathcal{DST}$ and $\mathcal{DCT}$. Filled spheres represent the k_z-grid of the respective transform. k is the discrete variable for the $\mathcal{DCT}$ (which equals the discretization variable in Fourier space) while k^* represents the discrete variable for the $\mathcal{DST}$ (which is related to the discretization variable in Fourier space by $k^* = k - 1$).

The discretizations in Fourier space for N grid points to calculate the weight functions, Eqs. (12) and (24), are

$$k_z^{\mathcal{DST}} = \frac{1}{2L_{\text{tot}}} [1, \ldots, N], \quad (B3a)$$

$$k_z^{\mathcal{DCT}} = \frac{1}{2L_{\text{tot}}} [0, \ldots, (N-1)]. \quad (B3b)$$

The $\mathcal{DST}$ does not include the (exact) value $\hat{\mathfrak{f}}_{k=0}^{\mathcal{DST}} = 0$, but instead considers $\hat{\mathfrak{f}}_{k=N}^{\mathcal{DST}}$, which the $\mathcal{DCT}$ does not include. This has been illustrated in Fig. 6. Therefore, the results of the $\mathcal{DST}$ and the $\mathcal{DCT}$ cannot be combined without modifications.

This has the following implications: $\hat{\rho}_i(k_z)$ in Eq. (29) (the result of the $\mathcal{DCT}$ from Eq. (25)) is multiplied by a vector-valued weight function. Because the $\mathcal{DST}$ is used to transform the product back to real space, the exact value $\hat{\mathfrak{f}}_{k=0}^{\mathcal{DCT}} = 0$ is disregarded, the sequence shifted and an approximate value for $\hat{\mathfrak{f}}_{k=N}^{\mathcal{DST}} \approx 0$ is added to the end of the sequence. This has a negligible effect on the results, because $\hat{\mathfrak{f}}_{k \to \infty}^{\mathcal{DST}} \to 0$ for smooth profiles. Eq. (31) has similar implications: the argument of the transform is the result of a $\mathcal{DST}$ transform, but is transformed back to real space by a $\mathcal{DCT}$ transform. Therefore, the exact value for $\hat{\mathfrak{f}}_{k=0}^{\mathcal{DCT}} = 0$ is the first element of the sequence, while the last element $\hat{\mathfrak{f}}_{k=N}$ is disregarded.

Appendix C: Iterative Solutions for the Density Profiles with Constraints

To constrain the total number of molecules N in the system can be used to increase the robustness of the numerical solution procedure.

Using the method of Rehner,[76] (Sec. 2.2) a semi-grand potential $\Omega^*([\{\rho_i(\mathbf{r})\}], T, N, \{\Delta\mu_i\})$, defined by

$$\Omega^*[\{\rho_i(\mathbf{r})\}] \equiv F[\{\rho_i(\mathbf{r})\}] - \sum_{i=2}^{N_c} \Delta\mu_i \int d\mathbf{r}' \, \rho_i(\mathbf{r}'), \quad (C1)$$

with $\Delta\mu_i \equiv \mu_i - \mu_1$ is utilized, which allows us to fix the total number of molecules N, and stabilize the vapor-liquid interface during the minimization. The Lagrangian is then

$$\mathcal{L}^* ([\{\rho_i(\mathbf{r})\}], \lambda) = \Omega^*[\{\rho_i(\mathbf{r})\}] + \lambda \left(N - \sum_{i=1}^{N_c} \int d\mathbf{r}' \, \rho_i(\mathbf{r}') \right), \quad (C2)$$

with a Lagrange multiplier λ that is equal to the chemical potential of the reference component, μ_1. The fixed-point equations become

$$\rho_j(\mathbf{r}) = z_j^{\text{b}} \exp\left(-\frac{\delta\beta F^{\text{res}}}{\delta\rho_j(\mathbf{r})} - \beta V_j^{\text{ext}}(\mathbf{r}) \right), \quad (C3)$$

$$z_j^{\text{b}} = \frac{N\Lambda_j^{-3} e^{\beta\Delta\mu_j}}{\sum_k \Lambda_k^{-3} e^{\beta\Delta\mu_k} \int d\mathbf{r} \, \exp\left(-\frac{\delta\beta F^{\text{res}}}{\delta\rho_k(\mathbf{r})} - \beta V_k^{\text{ext}}(\mathbf{r}) \right)}, \quad (C4)$$

where the bulk fugacity is given by

$$z_j^{\text{b}} = \exp(\beta\lambda) \Lambda_j^{-3} \exp(\beta\Delta\mu_j) = \rho_j^{\text{b}} \exp\left(\beta\mu_j^{\text{res,b}} \right). \quad (C5)$$

The combination of Eqs. (C3) and (C4) allows the DFT to be solved for multicomponent mixtures by specifying the total number of molecules N and the chemical potentials $\{\Delta\mu_i\}$. Note that fixing the number of molecules is not exacly equivalent to a canonical or semi-grand ensemble. Eq. (C4) merely enforces a solution of Eq. (C3) where the number of molecules in the system equals N.

REFERENCES

[1] H. Frisch and P. Nielaba, J. Chem. Phys. **105**, 7238 (1996).

[2] X. Zhao, J. K. Johnson, and C. E. Rasmussen, J. Chem. Phys. **120**, 8707 (2004).

[3] A. Ramiere, S. Volz, and J. Amrit, Nat. Mater. **15**, 512 (2016).

[4] A. Bauer, T. Mayer, M. Semmel, M. A. G. Morales, and J. Wind, Int. J. Hydrog. Energy **44**, 6795 (2019).

[5] Ø. Wilhelmsen, D. Berstad, A. Aasen, P. Nekså, and G. Skaugen, Int. J. Hydrog. Energy **43**, 5033 (2018).

[6] D. Berstad, G. Skaugen, and Ø. Wilhelmsen, Int. J. Hydrog. Energy **46**, 8014 (2021).

[7] G. Skaugen, D. Berstad, and Ø. Wilhelmsen, Int. J. Hydrog. Energy **45**, 6663 (2020).

[8] H. Oh, I. Savchenko, A. Mavrandonakis, T. Heine, and M. Hirscher, ACS nano **8**, 761 (2014).

[9] J. P. Toennies, A. F. Vilesov, and K. B. Whaley, Physics Today **54**, 31 (2001).

[10] J. Salazar, S. Lectez, C. Gauvin, M. Macaud, J. Bellat, G. Weber, I. Bezverkhyy, and J. Simon, Int. J. Hydrog. Energy **42**, 13099 (2017).

[11] J. M. McMahon, M. A. Morales, C. Pierleoni, and D. M. Ceperley, Reviews of modern physics **84**, 1607 (2012).

[12] D. M. Ceperley, Rev. Mod. Phys. **67**, 279 (1995).

[13] L. M. Sesé and R. Ledesma, J. Chem. Phys. **102**, 3776 (1995).

[14] L. M. Sesé and L. E. Bailey, J. Chem. Phys. **119**, 10256 (2003).

[15] Q. Wang and J. K. Johnson, Fluid Phase Equilib. **132**, 93 (1997).

[16] A. Gil-Villegas, A. Galindo, P. J. Whitehead, S. J. Mills, G. Jackson, and A. N. Burgess, J. Chem. Phys. **106**, 4168 (1997).

[17] E. Wigner, Phys. Rev. **40**, 749 (1932).

[18] J. G. Kirkwood, Phys. Rev. **44**, 31 (1933).

[19] R. P. Feynman, A. R. Hibbs, and D. F. Styer, *Quantum Mechanics and Path Integrals, Emended edition* (McGraw-Hill, New York, 2005) p. 384.

[20] A. V. A. Kumar, H. Jobic, and S. K. Bhatia, J. Phys. Chem. B **110**, 16666 (2006).

[21] F. Calvo, J. P. K. Doye, and D. J. Wales, J. Chem. Phys. **114**, 7312 (2001).

[22] R. Rodríguez-Cantano, R. Pérez de Tudela, M. Bartolomei, M. I. Hernández, J. Campos-Martínez, T. González-Lezana, P. Villarreal, J. Hernández-Rojas, and J. Bretón, J. Phys. Chem. A **120**, 5370 (2016).

[23] P. Kowalczyk, L. Brualla, P. Gauden, and A. P. Terzyk, Phys. Chem. Chem. Phys. **11**, 9182 (2009).

[24] V. M. Trejos, A. Gil-Villegas, and A. Martinez, J. Chem. Phys. **139**, 184505 (2013).

[25] A. Aasen, M. Hammer, Å. Ervik, E. A. Müller, and Ø. Wilhelmsen, J. Chem. Phys. **151**, 064508 (2019).

[26] A. Aasen, M. Hammer, E. A. Müller, and Ø. Wilhelmsen, J. Chem. Phys. **152**, 074507 (2020).

[27] A. Aasen, M. Hammer, S. Lasala, J.-N. Jaubert, and Ø. Wilhelmsen, Fluid Phase Equilib. **524**, 112790 (2020).

[28] J. Navarro, F. Ancilotto, M. Barranco, and M. Pi, J. Phys. Chem. A **115**, 6910 (2011).

[29] P. Rehner, A. Aasen, and Ø. Wilhelmsen, J. Chem. Phys. **151**, 244710 (2019).

[30] A. Aasen, D. Reguera, and Ø. Wilhelmsen, Phys. Rev. Lett. **124**, 045701 (2020).

[31] Ø. Wilhelmsen, T. T. Trinh, S. Kjelstrup, and D. Bedeaux, J. Phys. Chem. C **119**, 8160 (2015).

[32] C. Klink, C. Waibel, and J. Gross, Ind. Eng. Chem. Res. **54**, 11483 (2015).

[33] R. Stierle, C. Waibel, J. Gross, C. Steinhausen, B. Weigand, and G. Lamanna, Int. J. Heat Mass Transfer **151**, 119450 (2020).

[34] J. Eller and J. Gross, Langmuir **37**, 3538 (2021).

[35] E. Sauer and J. Gross, Ind. Eng. Chem. Res. **56**, 4119 (2017).

[36] J. Mairhofer and J. Gross, Fluid Phase Equilib. **439**, 31 (2017).

[37] E. Sauer, A. Terzis, M. Theiss, B. Weigand, and J. Gross, Langmuir **34**, 12519 (2018).

[38] P. J. Leonard, D. Henderson, and J. A. Barker, Trans. Faraday Soc. **66**, 2439 (1970).

[39] M. Hammer, A. Aasen, Å. Ervik, and Ø. Wilhelmsen, J. Chem. Phys. **152**, 134106 (2020).

[40] T. Lafitte, A. Apostolakou, C. Avendaño, A. Galindo, C. S. Adjiman, E. A. Müller, and G. Jackson, J. Chem. Phys. **139**, 154504 (2013).

[41] R. Stierle, E. Sauer, J. Eller, M. Theiss, P. Rehner, P. Ackermann, and J. Gross, Fluid Phase Equilib. **504**, 112306 (2020).

[42] Y. Rosenfeld, Phys. Rev. Lett. **63**, 980 (1989).

[43] R. Roth, R. Evans, A. Lang, and G. Kahl, J. Phys.: Condens. Matter **14**, 12063 (2002).

[44] T. Boublík, J. Chem. Phys. **53**, 471 (1970).

[45] G. Mansoori, N. F. Carnahan, K. E. Starling, and T. W. Leland, J. Chem. Phys. **54**, 1523 (1971).

[46] Y.-X. Yu and J. Wu, J. Chem. Phys. **116**, 7094 (2002).

[47] M. G. Knepley, D. A. Karpeev, S. Davidovits, R. S. Eisenberg, and D. Gillespie, J. Chem. Phys. **132**, 124101 (2010).

[48] R. Stierle and J. Gross, Fluid Phase Equilib. **511**, 112500 (2020).

[49] D. G. Anderson, J. ACM **12**, 547 (1965).

[50] D. G. Anderson, Numer. Algorithms **80**, 135 (2019).

[51] P. Pulay, Chem. Phys. Lett. **73**, 393 (1980).

[52] P. Pulay, J. Comput. Chem. **3**, 556 (1982).

[53] A. Kovalenko, S. Ten-no, and F. Hirata, J. Comput. Chem. **20**, 928 (1999).

[54] J. Mairhofer and J. Gross, Fluid Phase Equilib. **444**, 1 (2017).

[55] J. Mairhofer, B. Xiao, and J. Gross, Fluid Phase Equilib. **472**, 117 (2018).

[56] J. K. Percus, Phys. Rev. Lett. **8**, 462 (1962).

[57] J. Eller, T. Matzerath, T. van Westen, and J. Gross, J. Chem. Phys. **154**, 244106 (2021).

[58] A. P. Thompson, H. M. Aktulga, R. Berger, D. S. Bolintineanu, W. M. Brown, P. S. Crozier, P. J. in 't Veld, A. Kohlmeyer, S. G. Moore, T. D. Nguyen, R. Shan, M. J. Stevens, J. Tranchida, C. Trott, and S. J. Plimpton, Comp. Phys. Comm. **271**, 108171 (2022).

[59] P. Rehner and G. Bauer, Front. Chem. Eng. **3**, 758090 (2021).

[60] Institute of Thermodynamics and Thermal Process Engineering, University of Stuttgart, "FeOs - Framework for equations of state," https://github.com/feos-org (2021).

[61] Ø. Wilhelmsen, A. Aasen, G. Skaugen, P. Aursand, A. Austegard, E. Aursand, M. A. Gjennestad, H. Lund, G. Linga, and M. Hammer, Ind. Eng. Chem. Res. **56**, 3503 (2017).

[62] SINTEF Energy Research and NTNU, "Thermopack open source thermodynamics library," https://github.com/thermotools/thermopack/ (2020).

[63] A. Mulero, I. Cachadiña, and M. I. Parra, J. Phys. Chem. Ref. Data **41**, 14 (2012).

[64] J. W. Leachman, R. T. Jacobsen, S. G. Penoncello, and E. W. Lemmon, J. Phys. Chem. Ref. Data **38**, 721 (2009).

[65] I. A. Richardson, J. W. Leachman, and E. W. Lemmon, J. Phys. Chem. Ref. Data **43**, 013103 (2014).

[66] R. Katti, R. T. Jacobsen, R. B. Stewart, and M. Jahangiri, in *Advances in Cryogenic Engineering: Volume 31*, edited by R. W. Fast (Springer US, Boston, MA, 1986) pp. 1189–1197.

[67] V. Baidakov, K. Khvostov, and V. Skripov, Fiz. Nizk. Temp. **7**, 957 (1981).

[68] V. Baidakov and K. Khvostov, Sov. J. Low Temp. Phys. **8**, 233 (1982).

[69] E. A. Guggenheim, J. Chem. Phys. **13**, 253 (1945).

[70] V. Baidakov, Fiz. Nizk. Temp. **10**, 677 (1984).

[71] V. N. Grigorev and N. S. Rudenko, Sov. phys. JETP **20**, 4 (1965).

[72] C. G. Paine and G. M. Seidel, Phys. Rev. B **46**, 1043 (1992).

[73] C. Paine and G. Seidel, Phys. B: Condens. Matter **194–196**, 969 (1994).

[74] Y. P. Blagoi and V. V. Pashkov, Sov. phys. JETP **28**, 3 (1969).

[75] C. G. Paine and G. M. Seidel, Phys. Rev. B **50**, 3134 (1994).

[76] P. Rehner, *Interfacial Properties Using Classical Density Functional Theory: Curved Interfaces and Surfactants*, Ph.D. thesis, University of Stuttgart (2021).